

Proton Transfer in Nanoconfined Polar Solvents. 1. Free Energies and Solute Position

Shenmin Li[†] and Ward H. Thompson^{*,‡}

*Department of Chemistry and Chemical Engineering, Dalian University, Dalian 116622, PR China, and
Department of Chemistry, University of Kansas, Lawrence, Kansas 66045*

Received: October 31, 2004; In Final Form: January 19, 2005

The reaction free energy curves for a model phenol–amine proton-transfer system in a confined CH₃Cl solvent have been calculated by Monte Carlo simulations. The free energy curves, as a function of a collective solvent coordinate, have been obtained for several fixed reaction complex radial positions (based on the center-of-mass). A smooth, hydrophobic spherical cavity was used to confine the solvent, and radii of 10 and 15 Å have been considered. Quantum effects associated with the transferring proton have been included by adding the proton zero-point energy to the classical free energy. The results indicate the reaction complex position can be an important component of the reaction coordinate for proton-transfer reactions in nanoconfined solvents.

1. Introduction

Nanostructured materials have drawn increasing interest recently as potential vessels in which pools of solvent confined to nanoscale dimensions serve as an environment for chemical reactions.^{1–5} In particular, micro- and mesoporous catalysts,¹ reverse micelles,^{2,6–13} sol–gels,^{3,14–19} and supramolecular assemblies⁴ have been investigated. However, a significant obstacle is the lack of design principles for these materials as potential reaction media. That is, what properties should a confining framework have in order to facilitate a desired reaction or hinder an undesired one? The nanostructured systems that can currently be synthesized vary dramatically in size, shape, dimensionality of the confinement, flexibility, surface roughness, and surface chemistry. In addition, the chemical energetics and dynamics are frequently complex in these systems. Theory and simulation provide important avenues for exploration of potential design principles of these systems since the properties of the confining framework can be straightforwardly controlled and modified.^{5,8–10,20–27}

In this paper we investigate the effect of nanoscale confinement on a proton-transfer reaction in an aprotic polar solvent. Proton-transfer reactions in nanoconfined solvents are interesting to study for a number of reasons. First, they represent a class of reactions that is important in wide areas of chemistry and biology. Second, the proton-transfer process is strongly coupled to the solvent dynamics and should thus be strongly affected by confining the solvent. There have been some experimental studies that support this; the proton-transfer rate constant was found to decrease significantly upon confinement.^{28,29} Here we use Monte Carlo simulations to obtain the free energy surfaces governing the proton transfer in a model reaction system confined in spherical, hydrophobic nanocavities. In particular, the free energy as a function of a collective solvent reaction coordinate is calculated for different fixed positions of the center-of-mass of the reaction complex. Quantum effects associated with the proton are included by adding the proton zero-point energy to the classical free energy. In addition, the position distributions of the reactant and product complexes are

presented. Two cavity sizes are considered with radii of 10 and 15 Å. The results shed light on the possible mechanisms for proton-transfer (and other charge-transfer) reactions in confined polar solvents.

In this paper we present Monte Carlo simulations of a model proton-transfer system (loosely based on a phenol–amine reaction complex) in a methyl chloride solvent. This reaction, described in detail in section 2.1, is closely related to a standard system used as a test problem for methods for describing proton-transfer reactions.^{30–32} In the present work, the reaction complex and solvent are confined in a spherical, hydrophobic cavity with nanoscale dimensions as discussed in section 2.2. The details of the Monte Carlo simulations for obtaining free energy surfaces are described in section 3 and the results are presented and discussed in section 4. Finally, some concluding remarks are given in section 5.

2. System

2.1. Proton-Transfer Complex. We have carried out Monte Carlo simulations for a model proton-transfer reaction in a CH₃Cl solvent confined in spherical cavities. The solute reaction complex is roughly based on a model of a phenol–amine proton-transfer reaction developed by Borgis³⁰ and used by several others.^{31,32} The present system differs from that of Borgis in that we use a two valence bond (VB) state model³⁵ to account for the changes in the reaction complex electronic structure in response to solvent motions instead of switching functions. The two VB states are a “neutral” state of the form A–H···B and an “ionic” state of the form A[–]···H–B⁺. Thus, in the reactants (products) the reaction complex electronic wave function will have predominantly neutral (ionic) character. In the present calculations the heavy atom distance (e.g., O···N) is held fixed at $R_{ON} = 2.7$ Å so this is effectively an intramolecular proton-transfer reaction.

One potential advantage of a two valence bond state description is that the energy difference between the minima of the two VB states in vacuo is a parameter that can be easily varied. This allows tuning of the reaction endo/exothermicity, e.g., due to substituent effects or, relevant for the present model study, to generate a reactive potential in environments of different polarity.

[†] Dalian University.

[‡] University of Kansas.

TABLE 1: Parameters for the Interaction Models of the Proton-Transfer Reaction Complex and Solvent Molecules Used in the Monte Carlo Simulations^a

site	ϵ (kcal/mol)	σ (Å)	q	r_{ij} (Å)
Reaction Complex				
neutral state				
Ph-O	0.09495	3.5	-0.5	variable 2.7
H	0.0		+0.5	
NR ₃	0.09495	3.5	0.0	
ionic state				
Ph-O	0.09495	3.5	-1	variable 2.7
H	0.0		+0.5	
NR ₃	0.09495	3.5	+0.5	
Solvent				
CH ₃ Cl (ref 43)				
CH ₃	0.2364	3.775	+0.25	1.781
Cl	0.4145	3.48	-0.25	

^a The parameters ϵ and σ define the Lennard-Jones interactions, q the site charge, and r_{ij} the distance between the site listed and the first site; see eq 1.

TABLE 2: Parameters for the in Vacuo Potentials of the Neutral ($\alpha = N$) and Ionic ($\alpha = I$) States of the Proton-Transfer Reaction Complex^a

parameter	$\alpha = N$	$\alpha = I$
D_α (eV)	5.1	4.2
b_α (Å ⁻¹)	1.568	1.5
r_α^{eq} (Å)	0.9572	0.90
B_α (eV)	0.04	0.05
ΔV_0 (eV)		0.6

^a See eqs 3 and 4. The electronic coupling is $V_{\text{coup}} = 1.0$ eV.

The solute and solvent molecules interact through Lennard-Jones and Coulomb potentials. The interaction energy between two sites is given by

$$V_{ij} = 4\epsilon_{ij} \left[\left(\frac{\sigma_{ij}}{r_{ij}} \right)^{12} - \left(\frac{\sigma_{ij}}{r_{ij}} \right)^6 \right] + \frac{q_i q_j}{r_{ij}} \quad (1)$$

The Lennard-Jones parameters for the solute and solvent are given in Table 1 along with the charges for the solvent and the two solute VB states. At each step in the Monte Carlo simulation the electronic ground state of the reaction complex is obtained by solving the two-state Schrödinger equation $\mathbf{H}\psi_g = V_g\psi_g$ where

$$\mathbf{H} = \begin{pmatrix} V_N(\mathbf{Q}) & V_{\text{coup}} \\ V_{\text{coup}} & V_I(\mathbf{Q}) \end{pmatrix} \quad (2)$$

Here, $V_N(\mathbf{Q})$ and $V_I(\mathbf{Q})$ are the total potential energies at configuration \mathbf{Q} with the solute in the neutral and ionic VB states, respectively, and V_{coup} is the electronic coupling (given in Table 2 title). Specifically, the diagonal potential energies are given by $V_\alpha(\mathbf{Q}) = V_\alpha^0 + V_{\alpha-\text{solv}}(\mathbf{Q})$, $\alpha = N, I$, where $V_{\alpha-\text{solv}}(\mathbf{Q})$ is the solute-solvent and solvent-solvent interactions given by the sum over site-site interactions in eq 1. The in vacuo interaction potentials in the proton coordinate, V_α^0 , are given by

$$V_N^0(r_{\text{OH}}; R_{\text{ON}}) = D_N [1 - e^{-b_N(r_{\text{OH}} - r_N^{\text{eq}})}]^2 + \frac{B_N}{r_{\text{HN}}^6} \quad (3)$$

and

$$V_I^0(r_{\text{OH}}; R_{\text{ON}}) = \Delta V_0 + D_I [1 - e^{-b_I(r_{\text{HN}} - r_I^{\text{eq}})}]^2 + \frac{B_I}{r_{\text{OH}}^6} \quad (4)$$

where $r_{\text{HN}} = R_{\text{ON}} - r_{\text{OH}}$. The parameters for these potentials are given in Table 2.

2.2. Cavity Model. We use a model potential for the cavity in which the interactions of the solute and solvent molecules with the cavity wall involve only a Lennard-Jones term integrated over a continuum of material surrounding the spherical cavity;⁸⁻¹⁰ the wall interactions are parametrized by σ_{wall} and ϵ_{wall} which are taken to be 2.5 Å and 0.46 kcal/mol, respectively. The result is a potential energy that depends only on the distance of each interaction site in a molecule from the center of the cavity. In this work, the cavity radius, R_{cav} , is taken to be 10 and 15 Å. The density of the solution inside the cavity is taken to be approximately the same for these two cavity sizes. Note that the actual densities may be slightly different than these nominal densities since for a fixed cavity size it is not possible to attain an arbitrary density. The volume used in calculating this density is obtained by reducing the nominal cavity radius by $0.5\sigma_{\text{wall}}$ (σ_{wall} is the effective Lennard-Jones radius of the cavity wall) to approximately account for the excluded volume, a quantity that changes significantly with cavity size. It is important to note that due to the spherical symmetry, structural properties of molecules need only be examined as a function of radial coordinates.

3. Monte Carlo Simulations

The vibrationally adiabatic free energy curves are calculated in a two-step process.^{33,34} First, the electronically adiabatic, vibrationally diabatic free energy curves as a function of the solvent coordinate

$$\Delta E \leftrightarrow s(\mathbf{Q}) = V_g(\mathbf{Q}; r_R) - V_g(\mathbf{Q}; r_P) \quad (5)$$

are obtained from a purely classical Monte Carlo simulation. Here, V_g is the ground-state potential energy obtained by diagonalizing \mathbf{H} in eq 2. In this simulation, the proton position is held fixed at a value characteristic of the reactants, r_R , and the classical (Helmholtz) free energy of the reactants is calculated as

$$A_R^{\text{cl}}(\Delta E) = -k_b T \ln \left[\frac{\int \delta[\Delta E - s(\mathbf{Q})] e^{-\beta V_g(\mathbf{Q}; r_R)} d\mathbf{Q}}{\int e^{-\beta V_g(\mathbf{Q}; r_R)} d\mathbf{Q}} \right] \quad (6)$$

The classical free energy of the products can be obtained directly from this free energy by

$$A_P^{\text{cl}}(\Delta E) = A_R^{\text{cl}}(\Delta E) - \Delta E \quad (7)$$

as shown previously.^{36,37} To accurately calculate the free energy away from the minimum, we employ an umbrella sampling approach³⁶⁻³⁹ in which the Monte Carlo simulation is run under the potential

$$V_{\text{umb}}(\mathbf{Q}) = V_g(\mathbf{Q}) + \eta[V_g(\mathbf{Q}; r_P) - V_g(\mathbf{Q}; r_R)] \quad (8)$$

with $\eta = 0, 0.25, 0.5, 0.75$, and 1. Here, $V_g(\mathbf{Q}; r_P)$ is the electronic ground-state energy for solvent configuration \mathbf{Q} and a proton coordinate, r_P , that is representative of the products. Thus, the system samples configurations that range from equilibrium conditions for the reactants to equilibrium conditions for the products. The simulations for different values of η give free energy curves that overlap but differ by a constant; these curves are shifted to generate a continuous curve by matching the overlapping regions.

Each Monte Carlo simulation for a given value of η consists of an equilibration stage of 500 000 cycles (1 cycle = N_{mol} steps, N_{mol} = total number of solute and solvent molecules) and a data collection stage of 4 000 000 cycles. All simulations are run at a temperature of 250 K and a density of 0.8 g/cm³; this density gives $N_{\text{mol}} = 26$ and 103 for $R_{\text{cav}} = 10$ and 15 Å, respectively.

Second, the vibrationally adiabatic free energy curves are obtained by adding the proton vibrational zero-point energy (ZPE)

$$A_{\text{g}}^{\text{qm}}(\Delta E) = A_{\text{min}}^{\text{cl}}(\Delta E) + \text{ZPE}(\Delta E) \quad (9)$$

where $A_{\text{min}}^{\text{cl}}(\Delta E)$ is the smaller of $A_{\text{R}}^{\text{cl}}(\Delta E)$ and $A_{\text{P}}^{\text{cl}}(\Delta E)$. This is accomplished by extracting the proton potential at different values of the solvent coordinate, ΔE . Specifically, for a specific value of ΔE , solvent configurations are sampled from the simulation, and the proton potential, $V_{\text{g}}(\mathbf{Q};r)$, is mapped out for each of these configurations (with the solvent held fixed). We have found that the proton potential is effectively the same for all configurations corresponding to a particular value of ΔE (supporting the definition of the solvent coordinate). The vibrational Schrödinger equation is then solved for the proton potential at each solvent coordinate (using a sinc function discrete variable representation basis⁴⁰ with 180 grid points), and the resulting zero-point energy is added to the lowest vibrationally adiabatic energy level to obtain the final free energy curve. In this context, the Monte Carlo simulations with fixed proton position serve to map out the vibrationally diabatic free energies, $A_{\text{R}}^{\text{cl}}(\Delta E)$ and $A_{\text{P}}^{\text{cl}}(\Delta E)$, and obtain solvent configurations typical of a particular ΔE . The effect of proton delocalization is then included by calculating and adding the zero-point energy (this also determines the vibrationally adiabatic free energies). The approximation inherent in this approach is a Born–Oppenheimer separation between the proton and solvent coordinates.

4. Results and Discussion

4.1. Reaction Complex Position Distributions. The probability distributions of the reaction complex position in spherical cavities of radius 10 and 15 Å have been calculated in two cases. Specifically, simulations were carried out with the oxygen–hydrogen bond distance fixed at $r_{\text{OH}} = 0.95$ and 1.7 Å, i.e., constrained to be reactants and products, respectively. The reaction complex (center-of-mass) position probability distributions are presented in Figure 1. It is important to note that while the proton position is fixed in these simulations, the electronic structure of the reaction complex is free to respond to the solvent polarization. These simulations serve to identify the location in the cavity of the reactants and products. The effect of proton delocalization is neglected for these purposes; it is expected that this approximation will make only relatively small quantitative changes in the distributions.

The probability distribution for the reactant complex ($r_{\text{OH}} = 0.95$ Å) is peaked near the cavity wall while the distribution for the product complex ($r_{\text{OH}} = 1.7$ Å) is peaked in the cavity interior for both cavity sizes. Specifically, the reactant complex is most probably found at a distance of ~ 3.4 Å from the cavity wall, in the first solvent shell next to the wall. Further, the distribution is unimodal and sharply peaked. Clearly, the distribution for the $R_{\text{cav}} = 15$ Å cavity is slightly broader than that for $R_{\text{cav}} = 10$ Å.

The probability distribution for the product complex is peaked at a distance of ~ 6.9 Å for $R_{\text{cav}} = 10$ Å and ~ 7.1 Å for the 15

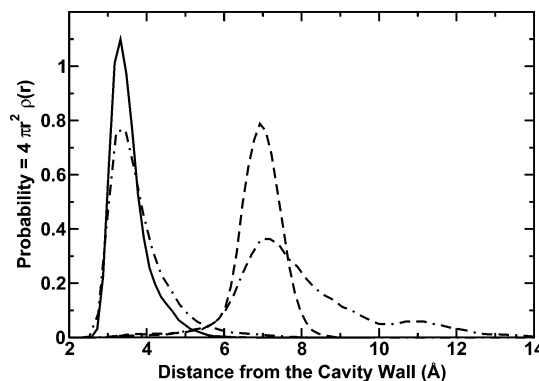


Figure 1. Proton-transfer reaction complex center-of-mass position probability density in a CH₃Cl solvent ($\rho = 0.8$ g/cm³) is shown as a function of distance from the cavity wall for two cavity sizes. In each case the proton position in the reaction complex, r_{OH} , is held fixed at a value characteristic of the reactants, 0.95 Å, or the products, 1.7 Å. Results are presented for a cavity radius of 10 Å with $r_{\text{OH}} = 0.95$ Å (solid line) and 1.7 Å (dashed line) and a radius of 15 Å with $r_{\text{OH}} = 0.95$ Å (dot–dashed line) and 1.7 Å (dot–dash–dashed line).

Å radius cavity. While the distribution in the smaller cavity is sharply peaked and unimodal, the distribution for $R_{\text{cav}} = 15$ Å is broader and displays a minor peak around 11 Å from the cavity wall. It is useful to note that the probability distribution involves both the radial density, $\rho(r)$, which is determined by the free energy of the reaction complex as a function of the radial position, and a geometric factor, $4\pi r^2$, that reflects the fact that there is more space for the reaction complex to be in nearer the cavity wall. The latter reduces the probability of finding the reaction complex near the center of the cavity. (It also is responsible for the sharp distributions for the reactant complex peaking near the cavity wall.)

The present results are consistent with previous simulations for a solute with a charge-transfer transition.²⁴ Namely, the solute with a large dipole moment (here, the product complex) is fully solvated in the cavity interior while the low dipole solute (here, the reactant complex) is partially solvated near the cavity wall. A key difference is that here the reaction complex is polarizable whereas in the previous work the solute had fixed charges. However, the present results indicate that this solute polarizability does not qualitatively affect the probability distributions. It is also important to note that the probability distributions are significantly affected by the solvent layering observed in these confined systems. In particular, in the 10 Å radius cavity the solvent sits in two molecular layers (solvent radial densities for the similar CH₃I solvent can be found in ref 25), and the reactant and product complex distributions are localized in the layer nearest and farthest from the cavity wall, respectively. The situation is similar in the larger cavity ($R_{\text{cav}} = 15$ Å) in which there are three layers, and the bimodal structure in the product complex distribution also reflects this solvent layering.

4.2. Reaction Free Energy Curves. The free energy curves for the proton-transfer system as a function of a collective solvent coordinate, eq 5, have been calculated for several fixed reaction complex positions (based on the center-of-mass), including the proton zero-point energy. The results for a 10 Å radius cavity are shown in Figure 2 while those for $R_{\text{cav}} = 15$ Å are plotted in Figure 3.

Consider first the smaller cavity results presented in Figure 2. The most notable result is that the free energy of reaction for the proton transfer is positive (endothermic) when the reaction complex is near the cavity wall but significantly negative (exothermic) when the reaction complex is in the cavity

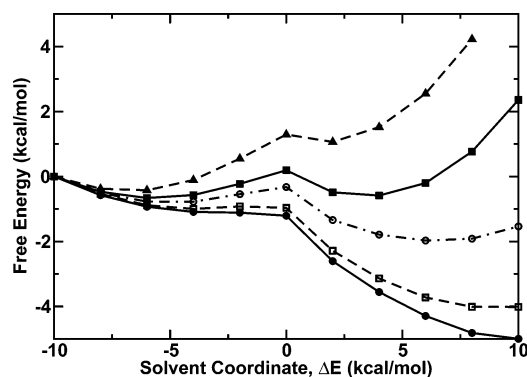


Figure 2. Reaction free energy curves for the model phenol–amine proton-transfer system are plotted vs the collective solvent coordinate, eq 5, for different reaction complex center-of-mass positions in a 10 Å radius cavity. Results are shown for distances from the cavity wall of $d = 3$ Å (dashed line with triangles), 4 Å (solid line with filled squares), 5 Å (dot-dashed line with open circles), 6 Å (dashed line with open squares), and 7 Å (solid line with filled circles). The free energy curves shown include the proton quantum zero-point energy (see the text).

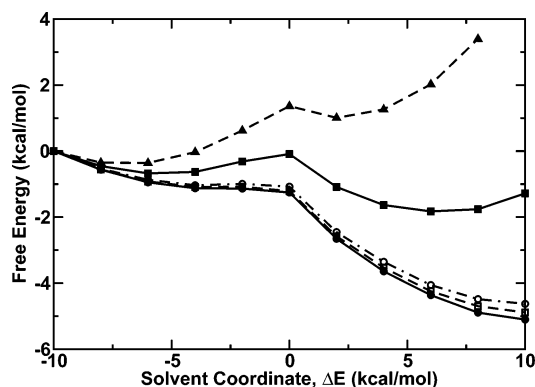


Figure 3. Same as Figure 2, except results are shown for a 15 Å radius cavity and distances from the cavity wall of $d = 3$ Å (dashed line with triangles), 5 Å (solid line with filled squares), 7 Å (dot-dashed line with open circles), 9 Å (dashed line with open squares), and 11 Å (solid line with filled circles).

interior. In fact, the free energy curves indicate that the position of the reaction complex “tunes” the reaction free energy almost continuously. (A nearly symmetric double well is observed for $d = 4$ Å, where d is the distance from the cavity wall.) The products exist as a weakly metastable local minimum for $d = 3$ Å which deepens and becomes the global minimum for $d = 5$ Å and the only minimum for larger values of d for which there is no minimum corresponding to reactants.

It is also noteworthy that the positions of the minima shift with the reaction complex position. Specifically, while the reactant minimum is difficult to identify for $d > 4$ Å, the product minimum shifts from $\Delta E_p^{\text{eq}} \sim 2$ kcal/mol for $d = 3$ Å to $\Delta E_p^{\text{eq}} > 10$ kcal/mol for $d = 7$ Å.

The results for $R_{\text{cav}} = 15$ Å presented in Figure 3 are in both qualitative and semiquantitative agreement with those for the 10 Å radius cavity. Specifically, the reaction free energy changes from positive to negative and the position of the product minimum moves to larger values of ΔE as the reaction complex position is changed from near the wall to the cavity interior. The key new feature is that as the reaction complex is moved beyond 7 Å from the cavity wall the changes in solvent polarity begin to saturate and significantly smaller changes are observed in the reaction free energy. Thus, the free energy curves for $d = 9$ and 11 Å are quite similar to that for 7 Å with the reaction free energy becoming slightly more negative with increasing

d . It is worth noting, however, that while the free energy curves appear to be “converging”, this system is almost certainly still far from the bulk solvent limit; evidence of this was found in previous simulations of the absorption and fluorescence spectra of a solute with a charge-transfer transition.²⁶

The dependence of the reaction free energy and location of the minima on the reaction complex position both indicate the variation of the effective solvent polarity within the cavity. In particular, the solvent is clearly more polar in the cavity interior than near the cavity wall. Furthermore, the change in solvent polarity experienced by the reaction complex at different positions is dramatic. Position-dependent solvent polarity has also been studied near planar interfaces.⁴¹ A few key differences here are that the solvent structure in these cavities are not governed by the same factors as for planar interfaces. Specifically, packing effects play a crucial role in determining the arrangement of the solvent molecules, leading, for example, to solvent molecules that line up parallel to the interface in these systems and to more dramatic solvent layering (see, e.g., refs 24–26). The resulting arrangement of solvent molecules has important consequences for the effective solvent polarity and the dynamics of solvent reorientation in the proton-transfer reaction coordinate. We have found that different solvents and densities can exhibit distinctly different structure in nanoconfined systems, so extrapolating details to other systems should be done with caution. However, the position dependence of the solvent polarity does appear to be general. Another issue is related to the bulk solvent limit. In the class of nanoconfined systems considered here the bulk limit is not reached as quickly as at bulk interfaces due to the absence of long-range electrostatic interactions; the role of such interactions in real nanostructured confining frameworks is not yet clear and likely system-dependent.

4.3. Classical and Quantum Contributions to the Free Energy. It is interesting to decompose the classical and quantum effects in the free energy curves presented in Figures 2 and 3. Since the proton quantum effects appear only in the zero-point energy added to the classical free energy, eq 9, this analysis is straightforward. To illustrate the proton quantum effects, the proton potential is shown in Figure 4 for three values of the solvent coordinate (for $R_{\text{cav}} = 10$ Å and $d = 5$ Å) along with the two lowest proton vibrational energy levels and eigenfunctions.

The results in Figure 4 have several notable features. First, as expected the minimum shifts from $r_{\text{OH}}^{\text{min}} \approx 0.95$ Å for $\Delta E = -6$ kcal/mol (reactants) through a nearly symmetric double-minimum potential for $\Delta E = 0$ kcal/mol (transition state) to $r_{\text{OH}}^{\text{min}} \approx 1.8$ Å for $\Delta E = 6$ kcal/mol (products). In each case there are two minima separated by a substantial barrier. Second, as a result of these changes in the proton potential with ΔE the ground-state vibrational eigenfunction shifts from a localized wave function in the O–H well through a delocalized wave function to a localized wave function in the H–N well for $\Delta E = -6, 0$, and 6 kcal/mol, respectively. Third, because of the delocalization of the wave function around the transition state, the zero-point energy is a minimum near $\Delta E = 0$ kcal/mol. This means that the proton quantum effects tend to suppress the barrier to proton transfer relative to the classical free energy; this has been noted in previous studies.^{32,33} This is illustrated in Figure 5 where the ZPE is plotted as a function of the solvent coordinate together with the classical and quantum free energy curves. Fourth, the vibrational energy levels at the transition state are below the barrier, indicating that proton tunneling should play an important role in the reaction dynamics for this

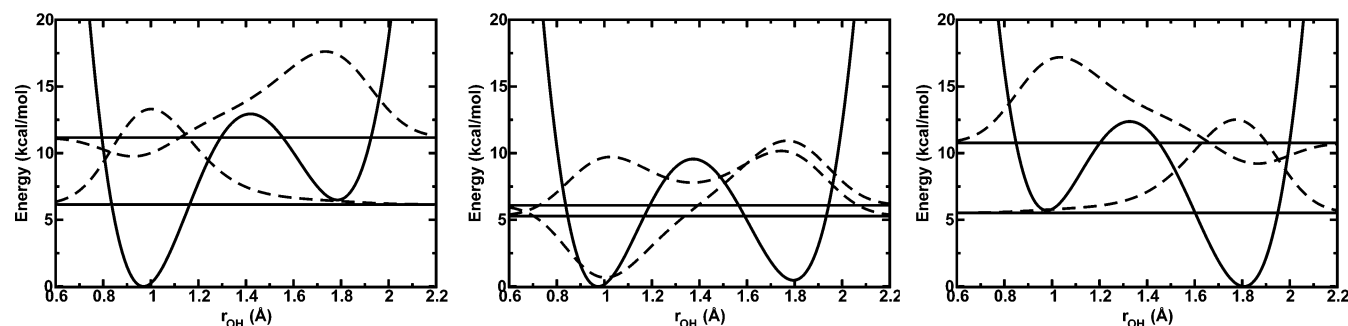


Figure 4. Proton potential (thick solid curve) is plotted vs r_{OH} along with the lowest two vibrational eigenvalues (horizontal solid lines) and eigenfunctions (dashed lines) for three values of the solvent coordinate, from left to right, $\Delta E = -6$, 0, and 6 kcal/mol. These three ΔE values correspond to reactants, the transition state, and products, respectively. All results are for $d = 5$ Å. (The eigenfunctions are scaled by a factor of 40.)

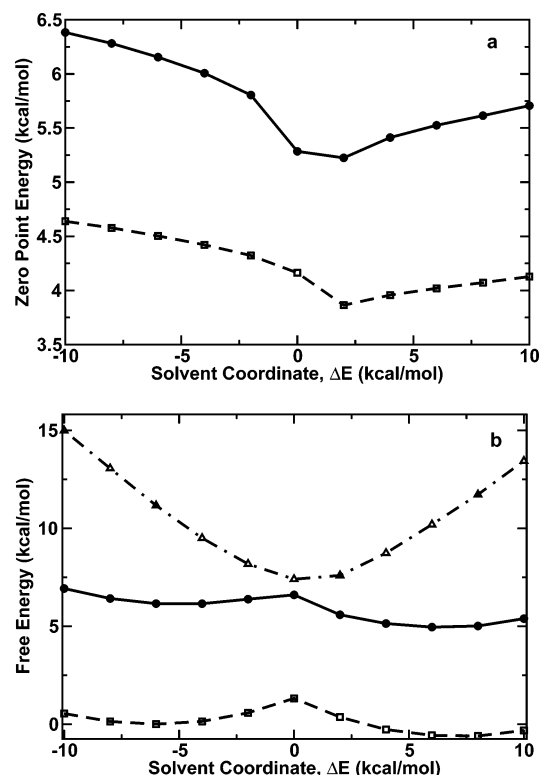


Figure 5. Proton (solid line with circles) and deuteron (dashed line with squares) zero-point energies are shown in panel a as a function of the solvent coordinate. The classical free energy (dashed line with squares) is shown in panel b as a function of the solvent coordinate with the quantum free energies obtained from adding the proton zero-point energy (solid line with circles) and the proton first excited-state vibrational energy (dot-dashed line with triangles). All results are for $d = 5$ Å.

model system. This is also supported by the small separation between the ground and excited vibrational energy levels at the transition state (see Figure 5); i.e., this is a nonadiabatic proton transfer.^{31,42} Fifth, the proton vibrational energy levels are essentially independent of the reaction complex position for all values of the solvent coordinate we have investigated. This is not surprising since the O–N distance is fixed in these simulations; this result may differ for an intermolecular proton-transfer reaction.

The effects associated with the quantum treatment of the proton motion can also be examined by isotopic substitution. The zero-point energy for the deuterated reaction complex is compared with the proton results in Figure 5. The proton quantum zero-point energy reduces the barrier from reactants

by ~ 0.9 kcal/mol while for the deuteron case the barrier is reduced by ~ 0.3 kcal/mol. The reaction free energy is also modified by including the zero-point energy since the O–H bond has a higher frequency, thus lowering the ΔA_{rxn} . The change is ~ 0.6 and ~ 0.4 kcal/mol for the proton and deuteron cases, respectively.

5. Conclusions

We have presented a Monte Carlo study of a model phenol–amine proton-transfer reaction in CH_3Cl confined in spherical hydrophobic spherical nanocavities. The reactant complex position distributions have been obtained for the reactants and the products, and the free energy curves for the reaction have been calculated for different complex center-of-mass positions. In addition, quantum effects associated with the proton have been included via the zero-point energy. Isotope effects have also been examined.

The key results of the present simulations are as follows for the proton-transfer model considered here: (1) The reactant proton-transfer complex is located near the cavity wall while the product complex is found primarily in the interior. (2) The reaction free energy depends strongly on the reaction complex position, varying from endothermic near the cavity wall to exothermic deep in the cavity interior. Together these demonstrate the reaction coordinate involves motion of the reaction complex from near the cavity wall to the interior. (3) There is not a strong dependence on cavity size. The results for the 15 Å radius cavity are in semiquantitative agreement with those for the 10 Å cavity. For the larger cavity the reaction endothermicity changes slowly for reaction complex positions beyond 7 Å from the cavity wall. (4) For this reaction system the proton zero-point energy is below the barrier at the transition state, indicating that tunneling will be significant in the reaction rate. This indicates that the reaction is a nonadiabatic proton transfer. (5) The proton quantum effects are not dependent on the reaction complex position in the cavity for this intramolecular proton-transfer reaction.

While these results strongly indicate that the reaction complex position is part of the reaction coordinate for proton transfer in these nanoconfined solvents, determining the details of the reaction mechanism will require molecular dynamics studies. We are currently carrying out such mixed quantum-classical dynamics simulations in which the proton is treated quantum mechanically, and the rest of the system is described classically in order to address this issue and investigate the effect of nanoscale confinement on the solvation dynamics relevant to proton transfer.

Acknowledgment. This work was supported by the Chemical Sciences, Geosciences and Biosciences Division, Office of Basic Energy Sciences, Office of Science, U.S. Department of Energy.

References and Notes

- (1) See, e.g.: De Vos, D. E.; Dams, M.; Sels, B. F.; Jacobs, P. A. *Chem. Rev.* **2002**, *102*, 3615–3640.
- (2) See, e.g.: Fendler, J. H. *J. Phys. Chem.* **1980**, *84*, 1485–1491. Pileni, M. P., Ed.; *Structure and Reactivity in Reverse Micelles*; Elsevier: New York, 1989.
- (3) Brinker, C. J.; Scherer, G. W. *Sol–Gel Science: The Physics and Chemistry of Sol–Gel Processing*; Academic Press: New York, 1990.
- (4) See, e.g.: Rebek, J., Jr. *Acc. Chem. Res.* **1999**, *32*, 278–286. MacGillivray, L. R.; Atwood, J. L. *Adv. Supramol. Chem.* **2000**, *6*, 157–183. Steed, J. W.; Atwood, J. L. *Supramolecular Chemistry*; Wiley: New York, 2000.
- (5) Bhattacharyya, K.; Bagchi, B. *J. Phys. Chem. A* **2000**, *104*, 10603–10613.
- (6) Sarkar, N.; Das, K.; Datta, A.; Das, S.; Bhattacharyya, K. *J. Phys. Chem.* **1996**, *100*, 10523–10527.
- (7) Riter, R. E.; Willard, D. M.; Levinger, N. E. *J. Phys. Chem. B* **1998**, *102*, 2705–2714. Pant, D.; Riter, R. E.; Levinger, N. E. *J. Chem. Phys.* **1998**, *109*, 9995–10003. Riter, R. E.; Undiks, E. P.; Kimmel, J. R.; Levinger, N. E. *J. Phys. Chem. B* **1998**, *102*, 7931–7938. Willard, D. M.; Riter, R. E.; Levinger, N. E. *J. Am. Chem. Soc.* **1998**, *120*, 4151–4160. Willard, D. M.; Levinger, N. E. *J. Phys. Chem. B* **2000**, *104*, 11075–11080. Pant, D.; Levinger, N. E. *Langmuir* **2000**, *16*, 10123–10130. Riter, R. E.; Undiks, E. P.; Levinger, N. E. *J. Am. Chem. Soc.* **1998**, *120*, 6062–6067. Riter, R. E.; Kimmel, J. R.; Undiks, E. P.; Levinger, N. E. *J. Phys. Chem. B* **1997**, *101*, 8292–8297.
- (8) Brown, D.; Clarke, J. H. R. *J. Phys. Chem.* **1988**, *92*, 2881–2888.
- (9) Linse, P. *J. Chem. Phys.* **1989**, *90*, 4992–5004. Linse, P.; Halle, B. *Mol. Phys.* **1989**, *67*, 537–573.
- (10) Faeder, J.; Ladanyi, B. M. *J. Phys. Chem. B* **2000**, *104*, 1033–1046. Faeder, J.; Ladanyi, B. M. *J. Phys. Chem. B* **2001**, *105*, 11148–11158.
- (11) Laria, D.; Kapral, R. *J. Chem. Phys.* **2002**, *117*, 7712–7718.
- (12) Senapati, S.; Keiper, J. S.; DeSimone, J. M.; Wignall, G. D.; Melnichenko, Y. B.; Frielinghaus, H.; Berkowitz, M. L. *Langmuir* **2002**, *18*, 7371–7376. Senapati, S.; M. L. Berkowitz, M. L. *J. Chem. Phys.* **2003**, *118*, 1937–1944. Senapati, S.; Berkowitz, M. L. *J. Phys. Chem. B* **2003**, *107*, 12906–12916.
- (13) Tobias, D. J.; Klein, M. L. *J. Phys. Chem.* **1996**, *100*, 6637–6648.
- (14) Zhang, J.; Jonas, J. *J. Phys. Chem.* **1993**, *97*, 8812–8815. Korb, J.-P.; Xu, S.; Jonas, J. *J. Chem. Phys.* **1993**, *98*, 2411–2422. Korb, J.-P.; Malier, L.; Cros, F.; Xu, S.; Jonas, J. *Phys. Rev. Lett.* **1996**, *77*, 2312–2315. Korb, J.-P.; Xu, S.; Cros, F.; Malier, L.; Jonas, J. *J. Chem. Phys.* **1997**, *107*, 4044–4050.
- (15) Loughnane, B. J.; Fourkas, J. T. *J. Phys. Chem. B* **1998**, *102*, 10288–10294. Loughnane, B. J.; Scodinu, A.; Fourkas, J. T. *J. Phys. Chem. B* **1999**, *103*, 6061–6068. Loughnane, B. J.; Farrer, R. A.; Scodinu, A.; Reilly, T.; Fourkas, J. T. *J. Phys. Chem. B* **2000**, *104*, 5421–5429. Farrer, R. A.; Fourkas, J. T. *Acc. Chem. Res.* **2003**, *36*, 605–612.
- (16) Streck, C.; Mel'nichenko, Y. B.; Richert, R. *Phys. Rev. B* **1996**, *53*, 5341–5347. Richert, R. *Phys. Rev. B* **1996**, *54*, 15762–15766.
- (17) Pal, S. K.; Sukul, D.; Mandal, D.; Sen, S.; Bhattacharyya, K. *J. Phys. Chem. B* **2000**, *104*, 2613–2616.
- (18) Wang, H.; Bardo, A. M.; Collinson, M. M.; Higgins, D. A. *J. Phys. Chem. B* **1998**, *102*, 7231–7237. Mei, E.; Bardo, A. M.; Collinson, M. M.; Higgins, D. A. *J. Phys. Chem. B* **2000**, *104*, 9973–9980.
- (19) Baumann, R.; Ferrante, C.; Deeg, F. W.; Bräuchle, C. *J. Chem. Phys.* **2001**, *114*, 5781–5791. Baumann, R.; Ferrante, C.; Kneuper, E.; Deeg, F. W.; Bräuchle, C. *J. Phys. Chem. A* **2003**, *107*, 2422–2430.
- (20) Nandi, N.; Bagchi, B. *J. Phys. Chem.* **1996**, *100*, 13914–13919.
- (21) Senapati, S.; Chandra, A. *J. Chem. Phys.* **1999**, *111*, 1223–1230.
- (22) Senapati, S.; Chandra, A. *J. Phys. Chem. B* **2001**, *105*, 5106–5109.
- (23) Turner, C. H.; Brennan, J. K.; Johnson, J. K.; Gubbins, K. E. *J. Chem. Phys.* **2002**, *116*, 2138–2148.
- (24) Thompson, W. H. *J. Chem. Phys.* **2002**, *117*, 6618–6628.
- (25) Thompson, W. H. *J. Chem. Phys.* **2004**, *120*, 8125–8133.
- (26) Gomez, J. A.; Thompson, W. H. *J. Phys. Chem. B* **2004**, *108*, 20144–20154.
- (27) Li, S.; Shepherd, T. D.; Thompson, W. H. *J. Phys. Chem. A* **2004**, *108*, 7347–7355.
- (28) Valeur, B.; Bardez, E. In *Structure and Reactivity in Reverse Micelles*; Pileni, M. P., Ed.; Elsevier: New York, 1989; pp 103–122.
- (29) Das, S.; Datta, A.; Bhattacharyya, K. *J. Phys. Chem. A* **1997**, *101*, 3299–3304. Mandal, D.; Pal, S. K.; Bhattacharyya, K. *J. Phys. Chem. A* **1998**, *102*, 9710–9714. Pal, S. K.; Mandal, D.; Bhattacharyya, K. *J. Phys. Chem. B* **1998**, *102*, 11017–11023.
- (30) Azzouz, H.; Borgis, D. *J. Chem. Phys.* **1993**, *98*, 7361–7375. Azzouz, H.; Borgis, D. *J. Mol. Liq.* **1995**, *63*, 89–107.
- (31) Hammes-Schiffer, S.; Tully, J. C. *J. Chem. Phys.* **1994**, *101*, 4567–4667.
- (32) Staib, A.; Borgis, D.; Hynes, J. T. *J. Chem. Phys.* **1995**, *102*, 2487–2505.
- (33) Warshel, A. *Computer Modelling of Chemical Reactions in Proteins and Solution*; Wiley: New York, 1991. Åqvist, J.; Warshel, A. *Chem. Rev.* **1993**, *93*, 2523–2544.
- (34) Ando, K.; Hynes, J. T. *J. Phys. Chem. B* **1997**, *101*, 10464–10478. Ando, K.; Hynes, J. T. *J. Phys. Chem. A* **1999**, *103*, 10398–10408.
- (35) Thompson, W. H.; Hynes, J. T. *J. Phys. Chem. A* **2001**, *105*, 2582–2590.
- (36) Warshel, A. *J. Phys. Chem.* **1982**, *86*, 2218–2224. King, G.; Warshel, A. *J. Chem. Phys.* **1990**, *93*, 8682–8692.
- (37) Ando, K.; Kato, S. *J. Chem. Phys.* **1991**, *95*, 5966–5982.
- (38) Allen, M. P.; Tildesley, D. J. *Computer Simulation of Liquids*; Oxford University Press: New York, 1987.
- (39) Frenkel, D.; Smit, B. *Understanding Molecular Simulation, from Algorithms to Applications*; Academic Press: New York, 1996.
- (40) Colbert, D. T.; Miller, W. H. *J. Chem. Phys.* **1992**, *96*, 1982–1991.
- (41) See, e.g.: Michael, D.; Benjamin, I. *J. Chem. Phys.* **2001**, *114*, 2817–2824. Vieceli, J.; Benjamin, I. *J. Phys. Chem. B* **2003**, *107*, 4801–4810. Vieceli, J.; Benjamin, I. *Chem. Phys. Lett.* **2004**, *385*, 79–84.
- (42) Borgis, D.; Hynes, J. T. *J. Phys. Chem.* **1996**, *100*, 1118–1128. Borgis, D.; Hynes, J. T. *Chem. Phys.* **1993**, *170*, 315–346. Borgis, D.; Hynes, J. T. *J. Chem. Phys.* **1991**, *94*, 3619–3628. Borgis, D.; Lee, S. Y.; Hynes, J. T. *Chem. Phys. Lett.* **1989**, *162*, 19–26.
- (43) Bigot, B.; Costa-Cabral, B. J.; Rivail, J. L. *J. Chem. Phys.* **1985**, *83*, 3083–3094.